

Modulation of surface properties on cobalt phosphide for high-performance ambient ammonia electrosynthesis

Qiangguo Meng^{a,1}, Yunpeng Hou^{b,1}, Fangqi Yang^a, Chenliang Cao^a, Zhi Zou^a, Junhui Luo^a, Weizhen Zhou^a, Zhikun Tong^a, Shixia Chen^a, Shaodong Zhou, Ph.D^{b,*}, Jun Wang, Ph.D^{a,*}, Shuguang Deng^c

^a School of Resource Environmental and Chemical Engineering, Nanchang University, Nanchang 330031, Jiangxi, China

^b College of Chemical and Biological Engineering, Zhejiang University, Hangzhou 310058, Zhejiang, China

^c School for Engineering of Matter, Transport and Energy, Arizona State University, 551 E. Tyler Mall, Tempe, AZ 85287, United States

ARTICLE INFO

Keywords:

N₂ fixation
in-situ Raman
Surface modulation
Cobalt phosphide
DFT calculation

ABSTRACT

Tuning surface properties of electrocatalysts for sustainable electrocatalytic nitrogen reduction reaction (NRR) with high selectivity and activity is highly demanded but still lacks fundamental understanding and modulation methods. Herein, we report the transformation of hydrogen evolution reaction (HER)-favorable cobalt phosphide (CoP) to NRR-favorable electrocatalyst via modulation of surface properties. The oxidized CoP particles encapsulated in carbon nanotubes (O-CoP/CNT) exhibits a high NH₃ yield of 39.58 µg h⁻¹ mg⁻¹ cat as well as high Faradaic efficiency (FE) of 19.4% at -0.5 V vs. reversible hydrogen electrode (RHE), which is confirmed by ¹⁵N₂ isotope-labeling tests. In-situ Raman spectra identify that N₂ molecules are preferentially captured by Co ions, while the surface-adsorbed H⁺ are gradually eliminated. The hydrophobic surface of CNT can limit the contact of protons with the catalyst surface to inhibit HER, and the formation of hydrogen bond facilitates a more efficient NRR process. The surface modulation effects are confirmed by density functional theory calculations.

1. Introduction

Ammonia (NH₃) is a fundamental chemical for the sustainable development of modern society because of its extensive usage of fertilizers and industrial chemicals [1]. Currently, more than 150 million tons of NH₃ are produced per year by the well-known Haber-Bosch process, which operates at high temperatures (300–500 °C) and pressures (20–50 MPa) [2]. This energy-intensive process takes up 1–2% of the total global energy consumption and concurrently releases an enormous amount of greenhouse gases [3]. Thus, artificial N₂ fixations under mild operation conditions have been persistently pursued to achieve high energy efficiency and environmental benignity [4]. Electrocatalytic N₂ reduction reaction (NRR) emerges as a promising alternative, which is powered by renewable electricity at ambient conditions without fossil fuel consumption and greenhouse gas emission [5,6]. Besides, NRR directly utilizes protons from water splitting instead of molecular H₂ [7]. However, the inertness of molecular nitrogen (with dissociation energy of 945 kJ mol⁻¹ for the N≡N bond) and the inevitable competing

hydrogen evolution reaction (HER) afford challenge for efficient NRR electrocatalysts with high activity and selectivity.

Among investigated electrocatalysts (e.g., transitional metals, heteroatoms-doped carbons, and single-atom catalysts) [8–10], transition metal phosphides (TMP), namely CoP, is promising for electro-reduction reactions due to its unique electronic structures with intrinsic charged character (Co^{δ+} and P^{δ-}) and has been demonstrated as an efficient HER electrocatalyst (Fig. 1a and b) [11–13]. Density functional theory (DFT) calculations revealed that the H* intermediate can be firmly adsorbed with an adsorption energy of 3.1 eV [14], and high proton concentrations near electrocatalyst surface are thus commonly observed [15]. On the other hand, the increased H* coverage can reinforce the adsorption and activation of N₂ on the surface of the CoP catalyst [16]. According to the “donation-acceptance” theory, the empty p-orbit of Co can accept the long-pair electrons of N₂, and the back donation from the Co 4s band to π* orbitalbos of N₂ molecules weakens the N≡N bonds [17]. These findings prompt us to further extend the application of CoP as an NRR electrocatalyst.

* Corresponding authors.

E-mail addresses: szhou@zju.edu.cn (S. Zhou), jwang7@ncu.edu.cn (J. Wang).

¹ These authors contributed equally to this work.

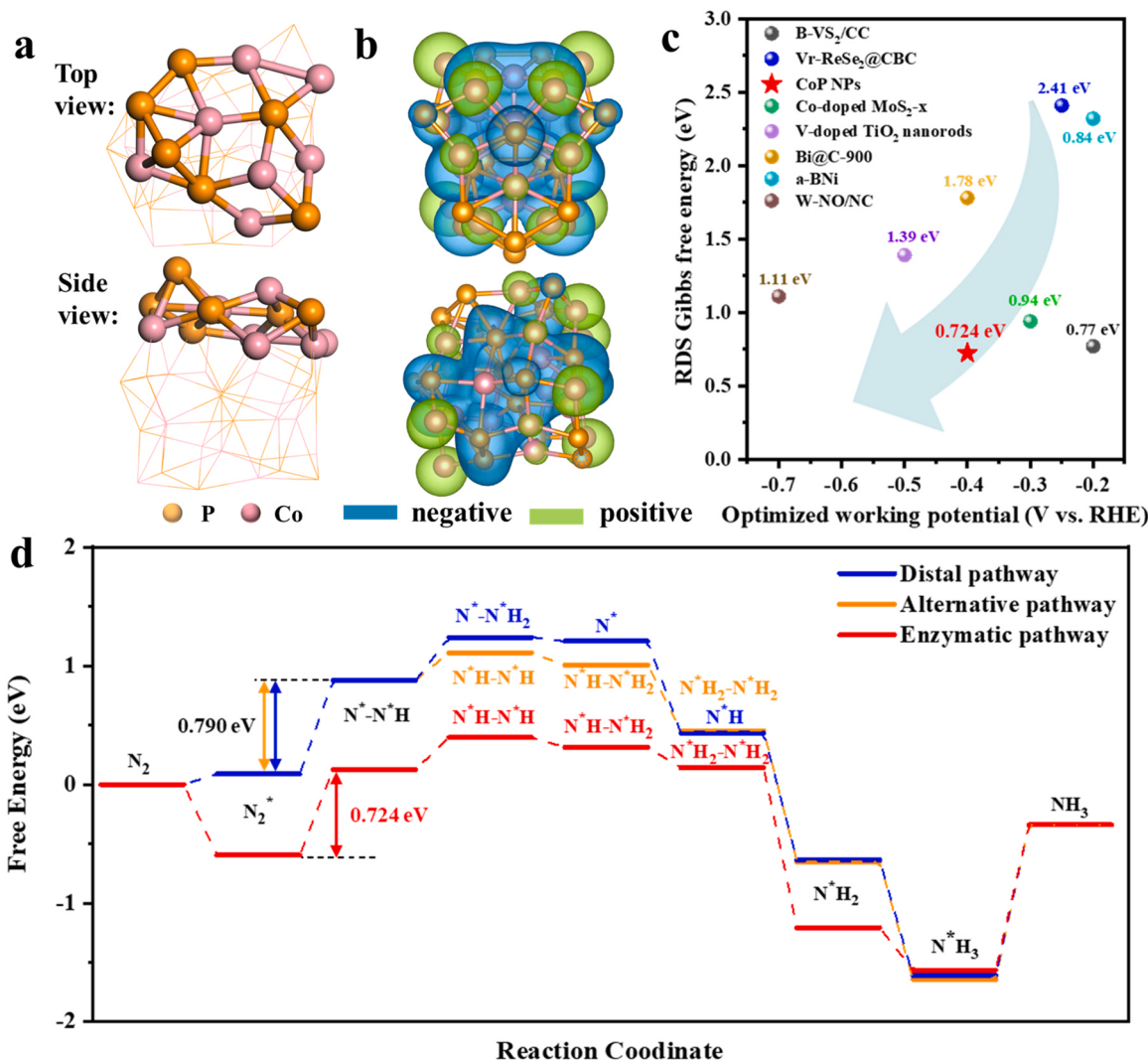


Fig. 1. (a) The atomic structure of CoP nanoparticles (CoP NPs): top view and side view; (b) Electronic deformation density for Co and P atoms: top view (above) and side view (below, isosurface level = 0.09 C/m); (c) Comparison chart of RDS Gibbs free energy of CoP with other top-ranking NRR electrocatalysts; (d) NRR free energy landscapes of distal, alternative, and enzymatic pathway.

We first conducted the DFT calculations to disclose the energetically preferred N_2 reduction route on the CoP catalyst and the associated mechanisms. From the calculated Gibbs free energy (ΔG) diagrams (Fig. 1d), N_2 molecules can be firmly adsorbed on the surface of CoP through the enzymatic pathway exothermically ($\Delta G_{N_2-N_2^*} = -0.597$ eV), contrasting to the weak N_2 adsorption through alternative and distal pathways. Considering the ultralow N_2 solubility in aqueous solution (0.6 mmol L⁻¹ at 25 °C and 1 atm) [18,19], the initial N_2 adsorption on the surface of CoP needs to be substantially enhanced to compete with the overwhelming HER. The initial hydrogenation step ($N_2^* \rightarrow N^*-N^*H$) is the common rate-determining step (RDS) of all three mechanisms, and the enzymatic pathway has the lowest RDS barrier of 0.724 eV. Even considering the computational uncertainty, this barrier is lower (or not higher) than the ones given by many top-ranking electrocatalysts, such as B-VS₂/CC (0.77 eV) [20], Vr-ReSe₂@CBC (2.41 eV) [21], Co-doped MoS_{2-x} (0.94 eV) [22], V-doped TiO₂ nanorods (1.39 eV) [23], Bi@C-900 (1.78 eV) [24], a-BNi (0.84 eV) [25], and W-NO/NC (1.11 eV, Fig. 1c) [26]. Therefore, benefitting from the enhanced N_2 adsorption and low N_2 activation barrier, CoP is capable of driving an efficient NRR process. In previous works, we have demonstrated the carbon-coating strategy to enhance the gas adsorption capacity and regulate the proton accessibility to electrocatalysts, resulting in depressed competing HER and improved CO₂RR and NRR activities [27,

28]. The combination of such a strategy and the CoP species, most likely, indicates a promising NRR electrocatalyst.

Herein, we demonstrate the preparation of in-situ confined CoP particles in carbon nanotubes (CoP/CNT) for the efficient NRR process for the first time. The introduction of oxygen moieties in the annealing and phosphating processes leads to the formation of oxygen-rich CoP clusters (O-CoP/CNT), which not only firmly anchor the cluster to the carbon nanotubes but also stabilize the NRR intermediates (i.e., N^*H-N^*H , $N^*H_2-N^*H$, and $N^*H_2-N^*H_2$) via additional hydrogen bonds thus enhancing the activity. The hydrophobic CNT coating can regulate the proton accessibility to selectively enhance the NRR activity. As a result, in 0.1 M Na₂SO₄ electrolyte, O-CoP/CNT delivers a high NH₃ yield of 39.58 µg h⁻¹ mg⁻¹ cat as well as high Faradaic efficiency (FE) of 19.4% at −0.5 V vs. reversible hydrogen electrode (RHE), which is confirmed by ¹⁵N₂ isotope-labeling experiments. *In-situ* Raman spectroscopy is applied to detect the reaction intermediates and identify the reaction pathway. Furthermore, the possible reaction mechanisms are revealed by DFT calculations.

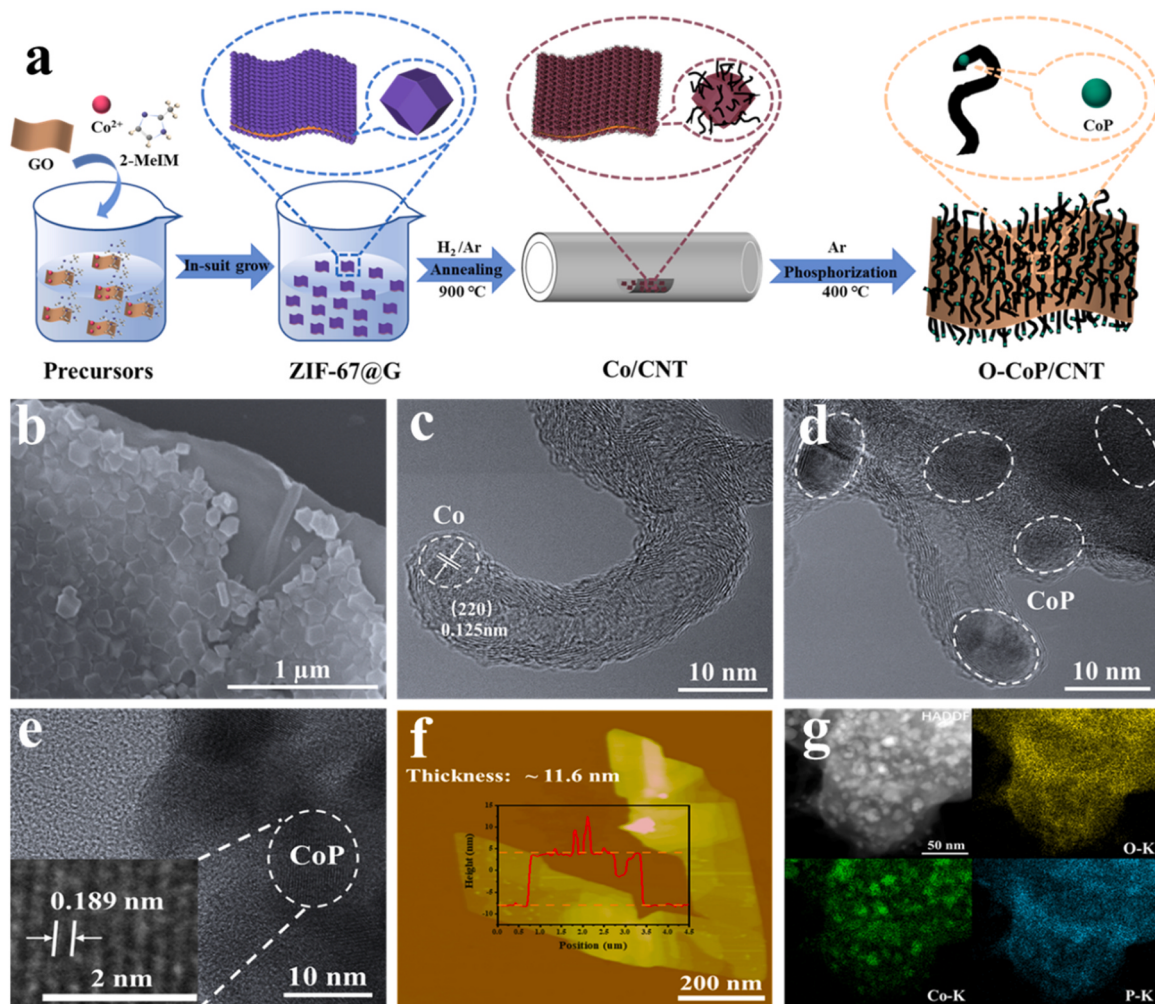


Fig. 2. (a) Schematic presentation of the synthesis process of O-CoP/CNT; (b) SEM image of ZIF-67@G; TEM image of (c) Co/CNT and (d) carbon nanotubes with embedded CoP nanoparticles; (e) HRTEM image, (f) AFM image, and (g) HADDF-STEM and EDS images of O-CoP/CNT.

2. Experimental section

2.1. Synthesis of ZIF-67@G

All chemical reagents were analytical grade and used without further purification. Initially, 4 mL graphene oxide (GO) solution (9.6 mg mL⁻¹) was dispersed in 20 mL methanol, then 40 mL 2-methylimidazole (1.314 g) methanol solution and 40 mL Co(NO₃)₂·6H₂O (582 mg) methanol solution were separately added into the GO solution. The mixture was kept stirring at room temperature for 4 h. After stirring, the mixture was standing overnight at room temperature. The product was obtained by centrifugation and washed with methanol at least five times. After freeze-drying overnight, the ZIF-67@G was obtained.

2.2. Preparation of O-CoP/CNT

Two quartz boats with the precursor Co/CNT (10 mg) and NaH₂PO₄ (100 mg) were placed in different positions in a tubular furnace under an Ar gas atmosphere. After annealing treatment at 400 °C with a heating rate of 3 °C min⁻¹ for 2 h, the black powdered O-CoP/CNT was obtained.

2.3. Electrochemical measurements

The electrochemical measurements were performed in a gas-tight H-type cell with three-electrodes separated by a proton-exchange

membrane (DuPont, Nafion 212). Before NRR measures, the Nafion 212 membrane was pretreated by heating in 0.5 M H₂SO₄ and 3 wt% H₂O₂ solutions at 80 °C for 2 h, respectively. And then put it into ultrapure water at 80 °C for 12 h. The H-shape electrochemical cell should also into ultrapure water at 80 °C for 12 h. All the electrochemical measurements were tested with a CHI660E electrochemical workstation (CH Instrument, China) in a three-electrode setup using a platinum plate (Pt, 1 cm × 1 cm) as the counter electrode, Ag/AgCl (saturated KCl solution) as the reference electrode, and O-CoP/CNT as the working electrode. All the electrochemical measurements were tested under ambient conditions. The catalyst inks were prepared by dispersing 2 mg catalyst powder into 350 μL of ethanol and 10 μL of Nafion (5 wt%) and 140 μL ultrapure water under ultrasonic for 1 h. And then dropped 50 μL of catalyst inks on carbon paper with 1 × 1 cm² used as the working electrode. The polarization curves were measured with a scan rate of 5.0 mVs⁻¹ at ambient conditions. Before NRR measurements, N₂ (99.99%) feeding gas was first purged through a 0.5 M H₂SO₄ solution and 0.5 M NaOH to eliminate the potential NO_x and NH₃ contaminants, and the electrolyte was also bubbled with high-purity N₂ for 30 min to expel the air. It should be pointed out that the N₂ was sufficiently purified to avoid the possible existence of NO_x in this work (Figs. S2a and b). In this work, all measured potential (vs. Ag/AgCl) were transformed into the potentials vs. reversible hydrogen electrode (RHE) via calibration with the following equation: E (vs. RHE) = E (vs. Ag/AgCl) + 0.197 + 0.059 × pH.

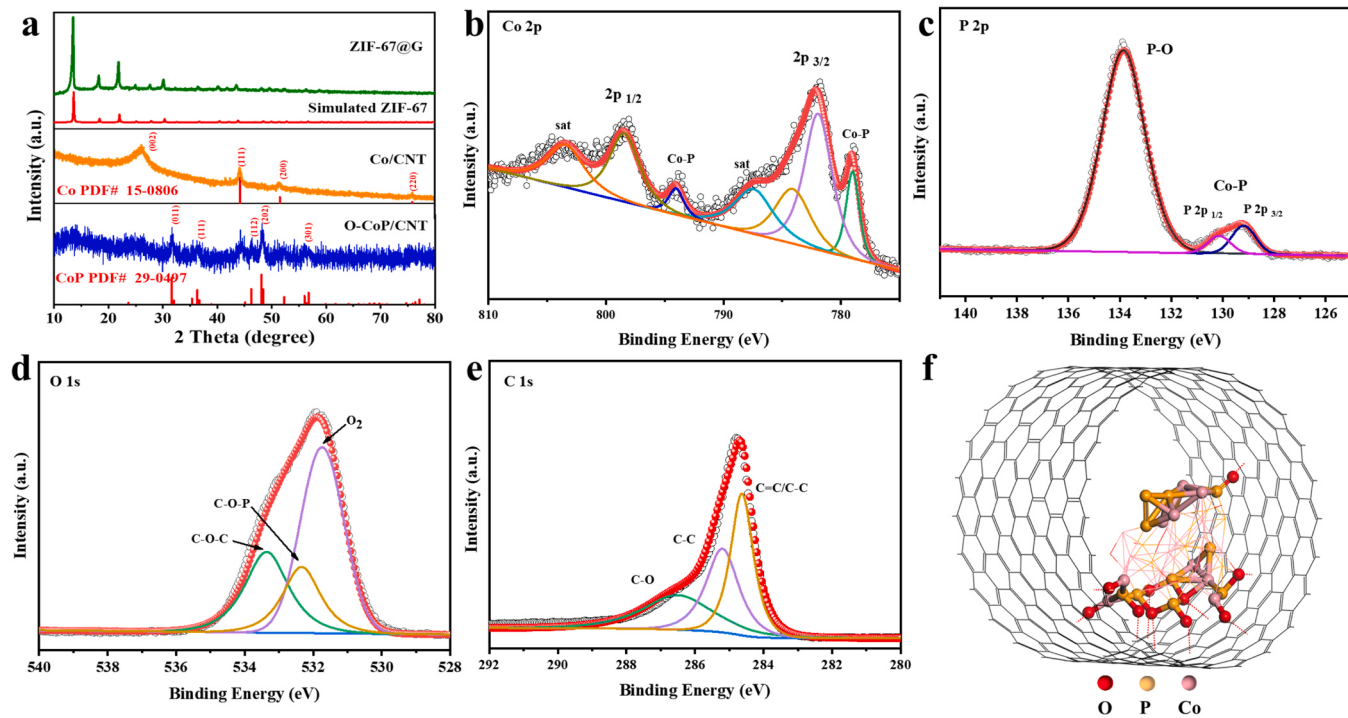


Fig. 3. (a) XRD patterns for ZIF-67@G, Co/CNT, and O-CoP/CNT; XPS spectra of (b) Co 2p, (c) P 2p, (d) O 1s, and (e) C 1s in O-CoP/CNT; (f) The schematic structure of O-CoP/CNT.

2.4. ^{15}N isotopic labeling experiment

$^{15}\text{N}_2$ was pre-purified by flowing through 0.5 M H_2SO_4 solution and 0.5 M NaOH solution to remove N contamination. Before NRR measurements, the electrolyte was also bubbled with high-purity $^{15}\text{N}_2$ which is purged for 30 min to expel the air. After electrolysis for 2 h, all the electrolyte (50 mL) in the cathode chamber was taken out, and its pH was adjusted to 3–4 by adding concentrated H_2SO_4 solution. The solution was evaporated under vacuum at 30 °C to become 2 mL. After that, 250 μL of electrolyte was mixed with 150 μL of D_2O , 50 μL of 3.5 mg mL^{-1} MA solution, and 50 μL of 0.05 M H_2SO_4 . The produced ammonia was quantified using ^1H nuclear magnetic resonance (NMR) measurements. Maleic acid (MA) was used for quantitative analysis.

2.5. Computational simulation details

In this work, all DFT calculations were performed at the GFN1-xTB level using the xTB program, version 6.3.2 [29].

For electronic self-consistent calculations, geometry optimizations and frequency calculations, the convergence tolerance is set as follows: integral cutoff = 0.20E + 02, Broyden damping = 0.40 and the accuracy = 5.0.

The free energy changes for different adsorptions were determined as follows:

$$\Delta G = E_{\text{ads}} - E_{\text{cluster}} + \Delta E_{\text{ZPE}} + \Delta H_{0 \rightarrow 300\text{K}} - T\Delta S$$

Here, E_{ads} is the electronic energy for adsorption states, E_{cluster} is the electronic energy of unadsorbed cluster, while ΔE_{ZPE} , $\Delta H_{0 \rightarrow 300\text{K}}$, and ΔS are zero-point energy change, thermal correction change from 0 to 300 K, and entropy change, which were also obtained through the xTB program, version 6.3.2.

3. Results and discussion

3.1. Synthesis and characterization of electrocatalysis

Fig. 2a schematically illustrates the three-step synthesis of modified CoP catalyst for NRR. The sacrificing template ZIF-67 was grown on thin two-dimensional (2D) graphene oxides (GO), by the examination of scanning electron microscope (SEM), regular polyhedral ZIF-67 particles are well dispersed on both sides of GO (Fig. 2b and S1). After annealing at 900 °C in the H_2/Ar (5:95, v/v) atmosphere, abundant CNTs were catalytically grown by metallic Co nanoparticles in the form of nanosphere, which are encapsulated in the head of CNTs (Co/CNT, Fig. 2c and S2). Upon phosphorization treatment, the polyhedral structure of ZIF-67 was completely destroyed due to the strong PH_3 etching (Fig. S3). The transmission electron microscope (TEM) image showed that CoP nanoparticles/nanospheres are embedded in multi-wall CNTs (O-CoP/CNT) and highlighted in Figs. 2d and S4. The lattice fringe of 0.189 nm was measured in the high-resolution TEM image (HRTEM) that corresponds to the (211) plane of CoP (Fig. 2e) [30]. Furthermore, the atomic force microscopy (AFM) image demonstrates that the average thickness of O-CoP/CNT is approximately 11.6 nm (Fig. 2f), the ultrathin 2D nanosheet will fully expose the active sites and facilitate the electron transfer [31]. The high-angle annular dark-field scanning TEM (HAADF-STEM) and the corresponding element mapping images corroborate the homogeneous distribution of O, P, and Co elements throughout the catalyst (Fig. 2g). The energy dispersive spectrum (EDS) indicates that the Co and P atomic ratio is nearly 1:1 (Fig. S5).

The phase transformations were collaboratively verified by powder X-ray diffraction (PXRD) patterns. As shown in Fig. 3a, ZIF-67@G showed identical diffraction peaks with simulated ZIF-67, whereas Co/CNT displayed diffraction peaks at 44.16°, 51.38°, and 75.89° that belong to the (111), (200), and (220) planes of metallic Co (JCPDS no. 15-0806). The (002) plane of graphitic carbon peak at 26.1° was also observed [32]. After the phosphorization, diffraction peaks at 31.6°, 36.3°, 46.2°, 48.4°, and 56.8° of O-CoP/CNT can be assigned to the (011), (111), (112), (202), and (301) planes of CoP (JCPDS no. 29-0497) [33],

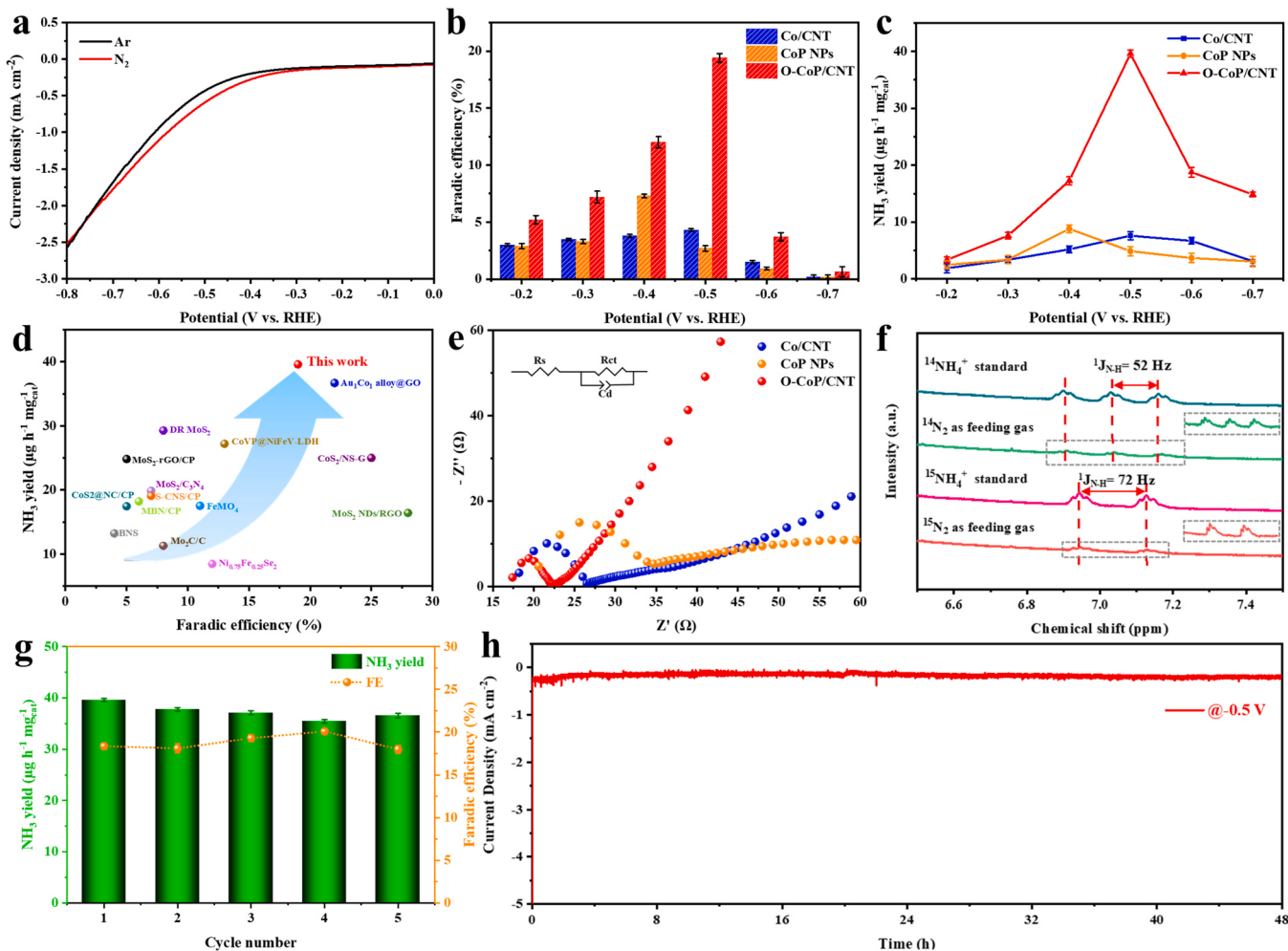


Fig. 4. (a) LSV curves of O-CoP/CNT in Ar- and N₂-saturated 0.1 M Na₂SO₄ solution; (b) NH₃ FE and (c) NH₃ yield rate at different potentials on CoP NPs, Co/CNT, and O-CoP/CNT; (d) NRR performance comparison chart of O-CoP/CNT and benchmark precious-metal-free NRR electrocatalyst; (e) EIS spectra of CoP NPs, Co/CNT, and O-CoP/CNT; (f) ¹H NMR spectra of the ¹⁵NH₄⁺ and ¹⁴NH₄⁺ standards and the NRR product using O-CoP/CNT catalyst in ¹⁴N₂ and ¹⁵N₂; (g) Cycling tests of O-CoP/CNT at -0.5 V; (h) Long-term experiments of O-CoP/CNT at -0.5 V for 48 h.

and the peak at 44.1° belongs to the slightly remained (111) plane of metallic Co. Besides, from N₂ adsorption-desorption isotherms at 77 K (Fig. S6), O-CoP/CNT showed a Brunauer-Emmett-Teller (BET) specific surface area of 45.2 m² g⁻¹, lower than that of Co/CNT (147.1 m² g⁻¹). The deceased specific surface area compared to Co/CNT can be caused by the destroyed polyhedral particles of Co/CNT and more generated defects due to the strong PH₃ etching. Raman spectra showed the disorder sp³ carbon (D band at 1359 cm⁻¹) and graphitic carbon (G band at 1587 cm⁻¹) [34,35], the absence of characteristic peaks of CoP is due to the complete carbon-coating on CoP catalyst (Fig. S7).

X-ray photoelectron spectroscopy (XPS) was employed to probe the chemical state of O-CoP/CNT (Fig. S8). In the high-resolution Co 2p spectrum (Fig. 3b), two binding peaks at 779.1 and 794.0 eV are assigned to the Co—P bond, indicating the successful formation of CoP [36,37]. The peaks at 781.2 eV and 798.4 eV and their corresponding shakeup satellite peaks at binding energies of 787.4 and 803.4 eV are assigned to Co-O bands [38]. Fig. 3c depicts the P 2p spectrum, two fitted peaks located at 129.2 and 130.1 eV are ascribed to the P 2p_{3/2} and P 2p_{1/2} in CoP, and another peak at 133.9 eV corresponds to P-O species [39,40]. The O 1s spectrum can be deconvoluted into three peaks at 531.8, 532.3, and 533.4 eV that belongs to the surface adsorbed oxygen species, C—O—P bond, and C—O—C bond, respectively (Fig. 3d) [41–43]. The C—O bond also exists in the C 1s spectra at 286.4 eV (Fig. 3e) [41]. Therefore, XPS results revealed that CoP nanoparticles

are immobilized and connected to the CNT walls by abundant O species (Fig. 3f).

3.2. Electrocatalytic NRR performances

To evaluate the NRR activities, the synthesized O-CoP/CNT electrocatalyst was tested in a two-compartment electrochemical cell filled with 0.1 M Na₂SO₄ aqueous electrolyte under ambient conditions. Before each test, high-purity N₂ gas (99.999%) successively went through acid and alkaline traps to remove possible NH₃ and NO_x impurities, and then constantly supplied to the cathode compartment at a flow rate of 30 cm³ min⁻¹. To identify the NRR products, NH₃ was spectrophotometrically quantified by the indophenol blue method [44], and the possible by-products of N₂H₄ and NO_x were detected using the Watt and Chrisp method and N-(1-naphthyl)-ethylenediamine dihydrochloride spectrophotometric method, respectively [45,46]. These standard calibration curves are presented in Figs. S9–S11. Hereafter, all potentials were converted to the RHE scale, unless otherwise noted. Fig. 4a showed the linear sweep voltammogram (LSV) curves of O-CoP/CNT in Ar- and N₂-saturated 0.1 M Na₂SO₄ electrolytes, and the latter exhibited a larger current density in the range of 0.0 ~ -0.8 V thus indicating considerable NRR activity [47]. All electroreduction reactions were conducted for 2 h at different potentials, while there is no N₂H₄ or NO_x can be detected under all potentials in post-electrocatalysis

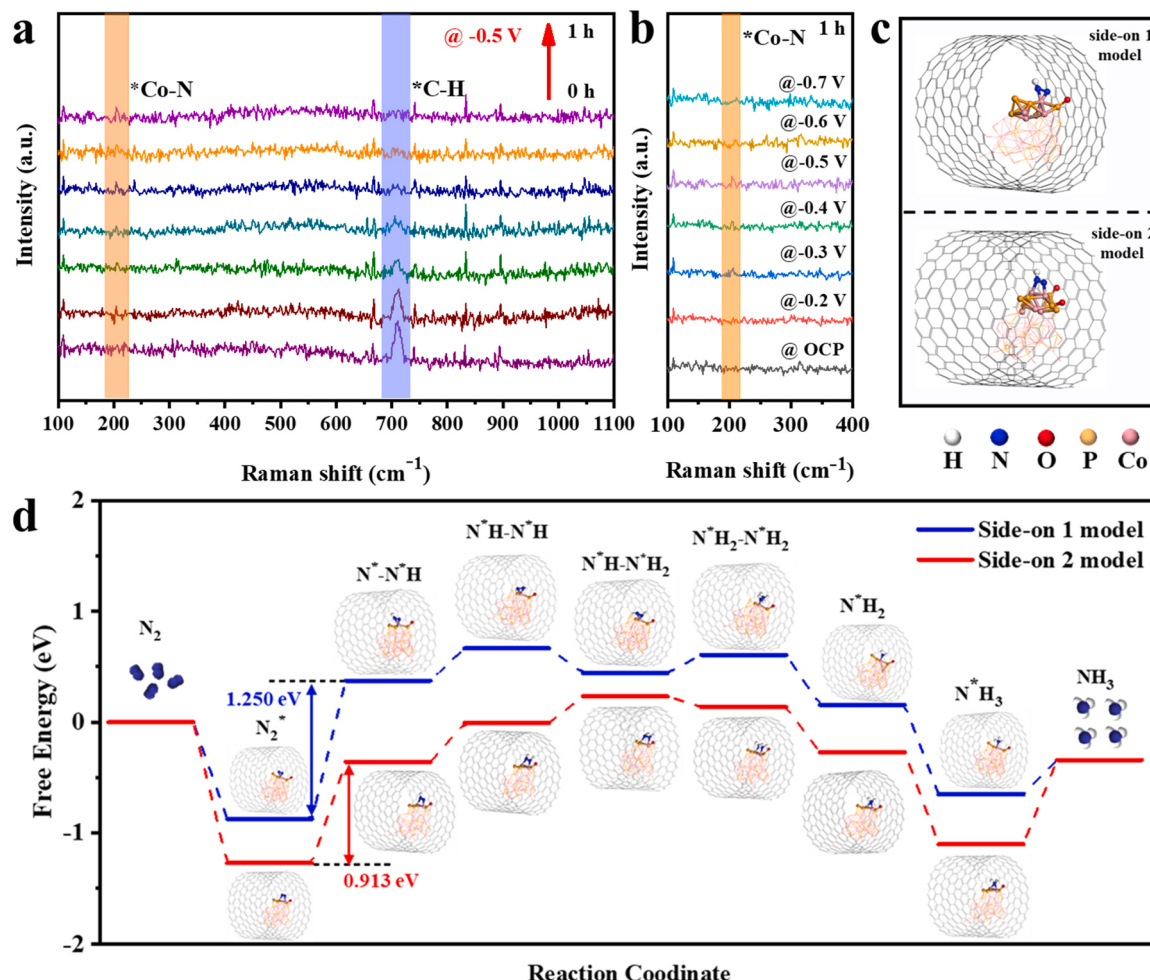


Fig. 5. *In-situ* Raman spectra of O-CoP/CNT (a) at -0.5 V from 0 to 1 h and (b) at various potentials from open circuit potential to -0.5 V; (c) The schematic structure of side-on 1 model (above) and side-on 2 model (below), (d) Free energy landscapes of side-on 1 and the side-on 2 pathways for O-CoP/CNT catalyst.

solutions, illustrating the excellent NH_3 selectivity (Figs. S12 and S13). To highlight the advantages of carbon-coating and CoP, the commercial CoP nanoparticles (CoP NPs, Fig. S14) and Co/CNT were used as references. The current density of O-CoP/CNT in N_2 -saturated 0.1 M Na_2SO_4 electrolyte was much higher than those of CoP NPs and Co/CNT (Figs. S15–S17), and the corresponding UV-vis absorption spectra are presented in Figs. S18–S20. As shown in Figs. 4b and c, both FE and yield of O-CoP/CNT increased with more negative potential applied from -0.2 V to -0.5 V. The highest NH_3 yield reaches $39.58 \mu\text{g h}^{-1} \text{mg}^{-1} \text{cat}$, corresponding to a FE of 19.4% at -0.5 V. As the potential moved to more negative, e.g., -0.6 V and -0.7 V, the FEs and yields both declined rapidly due to the gradually dominated HER [27]. In contrast, under the same conditions, inferior NH_3 yield and FE were obtained on either CoP NPs or Co/CNT: a maximal NH_3 yield of $8.81 \mu\text{g h}^{-1} \text{mg}^{-1} \text{cat}$ and FE of 7.3% at -0.4 V were found for CoP NPs (Fig. S21); the highest NH_3 yield of $7.6 \mu\text{g h}^{-1} \text{mg}^{-1} \text{cat}$ and FE of 4.3% at -0.5 V were obtained with Co/CNT (Fig. S22). We also prepared the P-doped CNT (P/CNT) without CoP nanoparticles to explore the effect of P atoms on NRR; and under the same conditions much inferior NH_3 yield of $9.1 \mu\text{g h}^{-1} \text{mg}^{-1} \text{cat}$ and FE of 8.6% at -0.4 V was obtained on P/CNT (Fig. S23). Moreover, the single Co atoms (Co SAs) may inevitably incorporate into the CNTs and contribute to NRR [9]. Thus, the poison experiment using KSCN solution was conducted to devitalize the Co SAs [34]. The O-CoP/CNT sample was dispersed within a 0.01 M KSCN solution for 30 min; in the following NRR experiment no deterioration of NH_3 FE and yield was observed, indicating that the Co SAs have a negligible contribution to NRR performances (Fig. S24). As the potential moves to more negative,

all NH_3 FEs and yields declined rapidly due to the gradually dominated HER [48]. The NRR performances on O-CoP/CNT are superior or comparable to the benchmark NRR electrocatalysts, such as CoVP@NiFeV-LDH (FE of 13.8%) [49], $\text{Ni}_{0.75}\text{Fe}_{0.25}\text{Se}_2$ (FE of 12.3%) [50], and FeMO_4 (FE of 10.5%) [51], the detailed comparison is depicted in Fig. 4d and summarized in Table S1. In the electrochemical impedance spectroscopy (EIS, Fig. 4e), O-CoP/CNT showed the lowest charge-transfer resistance (R_{ct}), confirming its high electronic conductivity [52]. The accessible electrochemically active surface areas (ECSA) were assessed by cyclic voltammetry (CV) curves of CoP NPs, Co/CNT, and O-CoP/CNT at varying scan rates from 20 to 120 mV s^{-1} (Fig. S25). The largest double-layer capacitance (C_{dl}) of 5.84 mF cm^{-2} was obtained on O-CoP/CNT, suggesting its more exposed sites for electrocatalytic NRR. Temperature-programmed desorption (TPD) measurements are carried out to investigate the N_2 adsorption strength. As shown in Fig. S26, O-CoP/CNT displayed the highest desorption temperature of 470 °C among three samples, implying its high N_2 adsorptive strength. Moreover, a more hydrophobic surface was observed on O-CoP/CNT with a larger electrolyte contact angle of 140° than that of Co/CNT (135°) and CoP NPs (65°), which can create abundant gas-filled gaps and increase the local N_2 concentration at the electrode/electrolyte interface (Fig. S27) [53].

To verify the origin of the NH_3 product during NRR, other possible N-containing species, e.g., NH_3 or NO_x , were excluded in the feeding N_2 gas (Fig. S28). Sufficient control experiments were conducted on O-CoP/CNT, including in the Ar-saturated solution at -0.5 V and in the N_2 -saturated solution at open circuit potential; consequently, no NH_3 can be

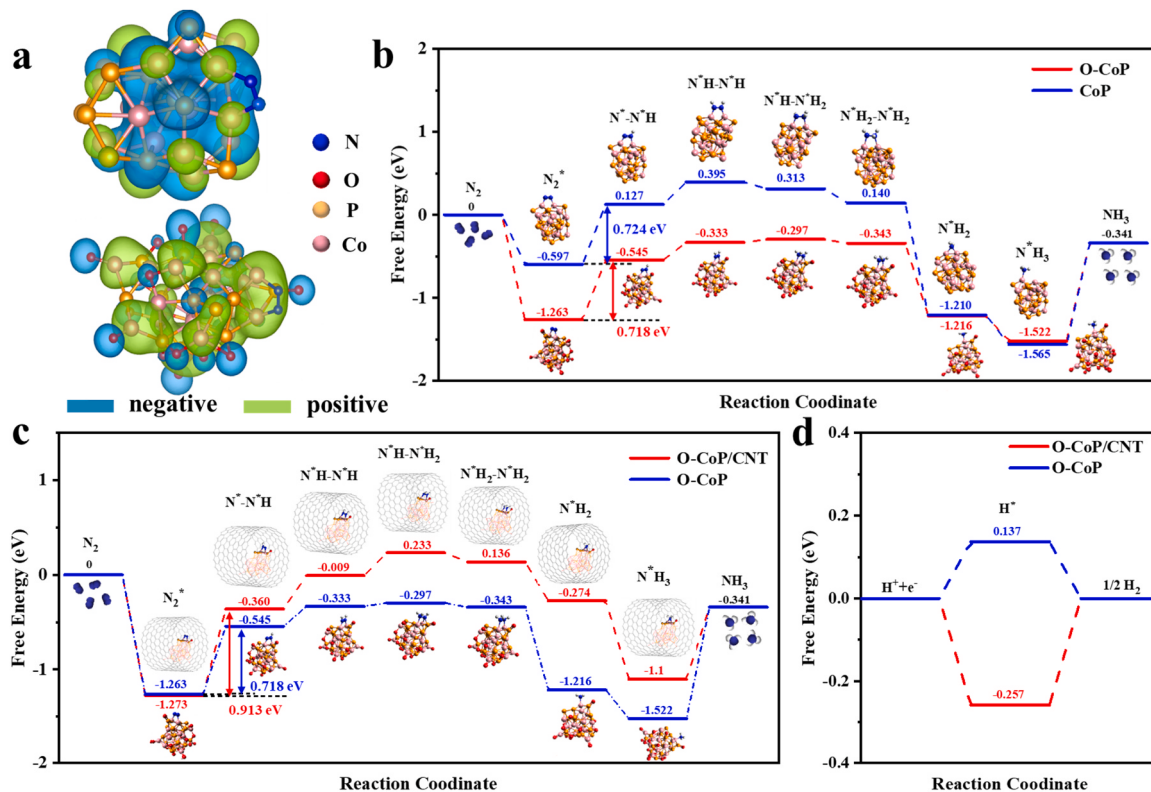


Fig. 6. (a) Electronic deformation density of CoP NPs (above) and O-CoP (below) after N₂ adsorption (isosurface level = 0.09 C/m); (b) Free energy landscapes for CoP NPs and O-CoP; (c) NRR and (d) HER free energy landscapes for O-CoP/CNT and O-CoP.

detected (Fig. S29) [54,55]. The carbon paper was also applied as the catalyst but no NH₃ was detected as well. Furthermore, ¹⁵N₂ isotope labeling experiments were performed, the ¹H nuclear magnetic resonance (NMR) spectra showed the dominating doublet coupling for ¹⁵NH₄⁺ and triplet coupling for ¹⁴NH₄⁺ (Fig. 4f) [56]. Quantitative analysis of NH₃ yields were calculated to be 37.84 μg h⁻¹ mg₁ cat and 38.48 μg h⁻¹ mg₁ cat at -0.5 V by ¹⁴NH₄⁺ and ¹⁵NH₄⁺ ¹H NMR spectra, respectively (Figs. S30 and S31) [57]. The almost identical yields confirmed that the NH₃ produced during NRR originates from N₂ feedstock.

Cycling stability of electrocatalyst is critical for the practical application, after five consecutive tests at -0.5 V, there are no marked deteriorations in either the NH₃ yield or the FE (Fig. 4g and S32). The NH₃ quantity increased linearly with the electrolysis time while the NH₃ FE kept stable (Fig. S33). Besides, the long-term stability of O-CoP/CNT was assessed by chronoamperometry measurements, which also showed no visible decay in current density during the 48-h continuous NRR process at -0.5 V (Fig. 4h). Moreover, the XRD patterns and TEM images of electrocatalyst before and after long-term electrolysis remained intact (Figs. S34 and S35). The XPS spectra after long-term cycling also showed no obvious change compared to the catalyst before the long-term NRR test (Figs. S36).

3.3. Study of reaction mechanisms

To identify the possible reaction intermediates during electrocatalysis and provide fundamental insights into the NRR mechanism, in-situ Raman measurements were carried out within different time ranges from 0 to 1 h at -0.5 V. As shown in Fig. 5a, at the very beginning (0 h), the strong characteristic peak of C—H bond at 720 cm⁻¹ is observed [58], implying that the surface of O-CoP/CNT was extensively covered by H⁺. With NRR proceeding, the C—H bond was gradually weakened and disappeared at 40 min, whereas a new characteristic peak at 215 cm⁻¹ emerged that can be assigned to the Co—N bond [59]. This

demonstrated that N₂ molecules are strongly adsorbed on the Co ions, which is confirmed by the stronger adsorption energy of N₂ (-1.12 eV) on the surface of CNT compared to that of H₂ (-0.92 eV, Fig. S37 and Table S2). Meanwhile, the adsorbed protons will be consumed in the production of NH₃ and molecular hydrogen; the coordination sites are then occupied by N₂ adsorption thus suppressing the HER process. In the potential-dependent in-situ Raman spectra (Fig. 5b), the strongest Co—N bond was observed at -0.5 V, consistent with the experimental results.

Based on the above findings, DFT calculations were carried out to reveal the reaction mechanism. Initially in the NRR process, the N₂ molecules can be captured by the Co ions via two possible configurations in the enzymatic pathway: side-on 1 model, in which two N atoms are bound to the same Co atom (Fig. 5c above); side-on 2 model, in which two N atoms coordinates to two adjacent Co atoms (Fig. 5c below). As shown in Fig. 5d, the formation of the first N—H bond (N₂^{*}→N^{*}-N^{*}H) is the rate-limiting for both pathways, and the side-on 2 model initiated route has a lower barrier of 0.913 eV. Further, we confirmed that the enzymatic mechanism from the side-on 2 adsorption is the energetically more preferred pathway, and the free energy diagrams via alternative and distal pathways are presented in Fig. S38. In contrast, the release of the first NH₃ (N^{*}-N^{*}H₂→N^{*}) is the common RDS for the alternative and distal pathways, and the barrier amounts to 1.893 eV and 1.153 eV, respectively.

To demonstrate the effects of the O atoms in enhancing the NRR activity, the electronic deformation density of CoP NPs and O-CoP after N₂ adsorption was analyzed (Fig. 6a). It turned out that the electron density at the nitrogen atoms is delocalized to the O atoms thus weakening the N≡N bond, which facilitates the formation of the N—H bonds. The DFT calculations were based on the side-on 2 model and the enzymatic route, along which the whole energy on O-CoP is located below that on CoP (Fig. 6b). This phenomenon can be attributed to the stabilization induced by the hydrogen bond formed between O and H atoms (Fig. S39); accordingly, the distances of the Co—N bonds are reduced to

1.725 and 1.722 Å on O-CoP compared to that on CoP (1.741 Å and 1.759 Å). As to the almost identical energy profiles for O-CoP and CoP after releasing the first NH₃, most likely, this is due to the absence of a hydrogen bond because the H atoms of *NH₂ are distant from the O atoms.

The O-CoP and O-CoP/CNT models are further applied to demonstrate the effect of CNT. The hydrophobic surface can overcome the mass transfer limitation of non-polar gases, and concentrate the gas molecules around the catalyst surface [27,28,60]. However, based on the free energy diagram in Fig. 6c, a higher barrier of the RDS step (0.913 eV) was found on O-CoP/CNT compared to 0.718 eV on O-CoP, indicating that the CNT coating decreases the activity of the catalyst regarding NRR. Higher theoretical overpotential is also required for O-CoP/CNT (Fig. S40). With respect to the HER processes, as shown in Fig. 6d, the energy barrier to generate H₂ on O-CoP/CNT (0.257 eV) is much higher than that on O-CoP (0.137 eV). This is because that the hydrophobic CNT coating can regulate the proton accessibility and selectively adsorb N₂ to efficiently inhibit HER. A higher NRR selectivity on O-CoP/CNT thus results.

4. Conclusion

In summary, we have demonstrated the modulation of surface properties of CoP by delicate preparation of O-CoP/CNT with hydrophobic surfaces and abundant O-moieties for high-performance NRR. Thus, O-CoP/CNT reached a high NH₃ yield of 39.58 μg h⁻¹ mg⁻¹ cat and FE of 19.4% at -0.5 V in 0.1 M Na₂SO₄, superior to the benchmark NRR catalysts. Moreover, it also exhibited remarkable long-term stability with no obvious current density decay for 48 h electrolysis. Sufficient control and ¹⁵N isotope labeling experiments have unambiguously confirmed the N source of NH₃ production. Furthermore, in-situ Raman spectroscopy detected reaction intermediates and identified the reaction pathway. DFT calculations revealed that the CNT coating can efficiently suppress HER due to its hydrophobic surface and more preferable N₂ adsorption, and the O-moieties can also effectively decrease the barrier of the rate-determining step (N₂*→N*-N*H). This work may guide and inspire future modification and design of efficient NRR catalysts.

CRediT authorship contribution statement

J.W., and Q.G.M. conceived the idea. J.W., Q.G.M., S.D.Z., Y.P.H., and S.G.D. drafted the manuscript. Q.G.M., C.L.G., and F.Q.Y. carried out the synthesis of materials and the electrochemical evaluation. Q.G. M., Z.Z., L.J.H., and W.Z.Z. helped with characterization of the materials. S.D.Z. and Y.P.H. conducted the DFT-D calculations. Z.K.T. and S. X.C. discussed the results and commented on the manuscript. J.W., S.D. Z., and S.G.D. revised the manuscript and supervised this project.

Declaration of Competing Interest

The authors declare that they have no known competing financial interests or personal relationships that could have appeared to influence the work reported in this paper.

Acknowledgements

This research work was supported by the National Natural Science Foundation of China (No. 21908090 and 21878265) and the Natural Science Foundation of Jiangxi Province (No. 20192ACB21015 and 20202BAB203010).

Appendix A. Supporting information

Supplementary data associated with this article can be found in the online version at doi:10.1016/j.apcatb.2021.120874.

References

- [1] J.G. Chen, R.M. Crooks, L.C. Seefeldt, K.L. Bren, R.M. Bullock, M.Y. Daresbourg, P.L. Holland, B. Hoffman, M.J. Janik, A.K. Jones, M.G. Kanatzidis, P. King, K. M. Lancaster, S.V. Lyman, P. Pfromm, W.F. Schneider, R.R. Schrock, Beyond fossil fuel-driven nitrogen transformations, *Science* 360 (2018) 6391.
- [2] C.J. van der Ham, M.T. Koper, D.G. Hetterscheid, Challenges in reduction of dinitrogen by proton and electron transfer, *Chem. Soc. Rev.* 43 (2014) 5183–5191.
- [3] W. Ye, M. Arif, X. Fang, M.A. Mushtaq, X. Chen, D. Yan, Efficient photoelectrochemical route for the ambient reduction of N₂ to NH₃ based on nanojunctions assembled from MoS₂ nanosheets and TiO₂, *ACS Appl. Mater. Interfaces* 11 (2019) 28809–28817.
- [4] Y. Li, J. Li, J. Huang, J. Chen, Y. Kong, B. Yang, Z. Li, L. Lei, G. Chai, Z. Wen, L. Dai, Y. Hou, Boosting electroreduction kinetics of nitrogen to ammonia via tuning electron distribution of single-atomic iron sites, *Angew. Chem. Int. Ed.* 60 (2021) 9078–9085.
- [5] M.A. Mushtaq, M. Arif, X. Fang, G. Yasin, W. Ye, M. Basharat, B. Zhou, S. Yang, S. Ji, D. Yan, Photoelectrochemical reduction of N₂ to NH₃ under ambient conditions through hierarchical MoSe₂@g-C₃N₄ heterojunctions, *J. Mater. Chem. A* 9 (2021) 2742–2753.
- [6] J. Wen, L. Zuo, H. Sun, X. Wu, T. Huang, Z. Liu, J. Wang, L. Liu, Y. Wu, X. Liu, T. V. Re, Nanomaterials for nitrogen electrochemical reduction reactions under ambient conditions, *Nanoscale Adv.* 3 (2021) 5525–5541, <https://doi.org/10.1039/DINA00426C>.
- [7] R. Zhao, H. Xie, L. Chang, X. Zhang, X. Zhu, X. Tong, T. Wang, Y. Luo, P. Wei, Z. Wang, X. Sun, Recent progress in the electrochemical ammonia synthesis under ambient conditions, *EnergyChem* 1 (2019) 100011.
- [8] Y. Fang, Z. Liu, J. Han, Z. Jin, Y. Han, F. X, Y. Niu, Y. Wu, Y. Xu, High-performance electrocatalytic conversion of N₂ to NH₃ using oxygen-vacancy-rich TiO₂ in situ grown on Ti₃C₂T_x MXene, *Adv. Energy Mater.* 9 (2019), 1803406.
- [9] Z. Liu, T. Hung, H. Chang, F. Wang, J. Wen, H. Sun, M. Hossain, Q. Xie, Y. Zhao, Y. Wu, Computational design of single Mo atom anchored defective boron phosphide monolayer as a high-performance electrocatalyst for the nitrogen reduction reaction, *Energy Environ. Mater.* 4 (2021) 255–262.
- [10] L. Xia, X. Wu, Y. Wang, Z. Niu, Q. Liu, T. Li, X. Shi, A.M. Asiri, X. Sun, S-doped carbon nanospheres: an efficient electrocatalyst toward artificial N₂ fixation to NH₃, *Small, Methods* 3 (2018), 1800251.
- [11] W. Guo, Z. Liang, J. Zhao, B. Zhu, K. Cai, R. Zou, Q. Xu, Hierarchical cobalt phosphide hollow nanocages toward electrocatalytic ammonia synthesis under ambient pressure and room temperature, *Small Methods* 2 (2018), 1800204.
- [12] E.J. Popczun, C.G. Read, C.W. Roske, N.S. Lewis, R.E. Schaak, Highly active electrocatalysis of the hydrogen evolution reaction by cobalt phosphide nanoparticles, *Angew. Chem. Int. Ed.* 53 (2014) 5427–5430.
- [13] J. Li, H. Liu, W. Gou, M. Zhang, Z. Xia, S. Zhang, C. Chang, Y. Ma, Y. Qu, Ethylene-glycol ligand environment facilitates highly efficient hydrogen evolution of Pt/CoP through proton concentration and hydrogen spillover, *Energy Environ. Sci.* 12 (2019) 2298–2304.
- [14] H. Song, M. Wu, Z. Tang, J.S. Tse, B. Yang, S. Lu, Single atom ruthenium-doped CoP/CDs nanosheets via splicing of carbon-dots for robust hydrogen production, *Angew. Chem. Int. Ed.* 60 (2021) 7234–7244.
- [15] C. Zhang, Y. Huang, Y. Yu, J. Zhang, S. Zhuo, B. Zhang, Sub-1.1 nm ultrathin porous CoP nanosheets with dominant reactive {200} facets: a high mass activity and efficient electrocatalyst for the hydrogen evolution reaction, *Chem. Sci.* 8 (2017) 2769–2775.
- [16] C. Ling, Y. Zhang, Q. Li, X. Bai, L. Shi, J. Wang, New mechanism for N₂ reduction: the essential role of surface hydrogenation, *J. Am. Chem. Soc.* 141 (2019) 18264–18270.
- [17] D. Yao, C. Tang, L. Li, B. Xia, A. Vasileff, H. Jin, Y. Zhang, S. Qiao, In situ fragmented bismuth nanoparticles for electrocatalytic nitrogen reduction, *Adv. Energy Mater.* 33 (2020), 2001289.
- [18] C.S.M. Kang, X. Zhang, D.R. MacFarlane, Synthesis and physicochemical properties of fluorinated ionic liquids with high nitrogen gas solubility, *J. Phys. Chem. C* 122 (2018) 24550–24558.
- [19] R. Battino, T.R. Rettich, T. Tominaga, The solubility of nitrogen and air in liquids, *J. Phys. Chem. Ref. Data* 13 (1984) 563–600.
- [20] Q. Li, Y. Guo, Y. Tian, W. Liu, K. Chu, Activating VS₂ basal planes for enhanced NRR electrocatalysis: the synergistic role of S-vacancies and B dopants, *J. Mater. Chem. A* 8 (2020) 16195–16202.
- [21] F. Lai, W. Zong, G. He, Y. Xu, H. Huang, B. Weng, D. Rao, J.A. Martens, J. Hofkens, I.P. Parkin, T. Liu, N₂ electroreduction to NH₃ via selenium vacancy-rich ReSe₂ catalysis at an abrupt interface, *Angew. Chem. Int. Ed.* 59 (2020) 13320–13327.
- [22] J. Zhang, X. Tian, M. Liu, H. Guo, J. Zhou, Q. Fang, Z. Liu, Q. Wu, J. Lou, Cobalt-modulated molybdenum–dinitrogen interaction in MoS₂ for catalyzing ammonia synthesis, *J. Am. Chem. Soc.* 141 (2019) 19269–19275.
- [23] T. Wu, W. Kong, Y. Zhang, Z. Xing, J. Zhao, T. Wang, X. Shi, Y. Luo, X. Sun, Greatly enhanced electrocatalytic N₂ reduction on TiO₂ via V doping, *Small Methods* 3 (2019), 1900356.
- [24] Y. Wan, H. Zhou, M. Zheng, Z.H. Huang, F. Kang, J. Li, R. Lv, Oxidation state modulation of bismuth for efficient electrocatalytic nitrogen reduction to ammonia, *Adv. Funct. Mater.* 31 (2021), 2100300.
- [25] Z. Fang, P. Wu, Y. Qian, G. Yu, Gel-derived amorphous bismuth–nickel alloy promotes electrocatalytic nitrogen fixation via optimizing nitrogen adsorption and activation, *Angew. Chem. Int. Ed.* 60 (2021) 4275–4281.
- [26] Y. Gu, B. Xi, W. Tian, H. Zhang, Q. Fu, S. Xiong, Boosting selective nitrogen reduction via geometric coordination engineering on single-tungsten-atom catalysts, *Adv. Mater.* 23 (2021), 2100429.

- [27] W. Yu, F. Shu, Y. Huang, F. Yang, Q. Meng, Z. Zou, J. Wang, Z. Zeng, G. Zou, S. Deng, Enhanced electrocatalytic nitrogen reduction activity by incorporation of carbon layer on SnS microflowers, *J. Mater. Chem. A* 8 (2020) 20677–20686.
- [28] S. Chen, Y. Li, Z. Bu, F. Yang, J. Luo, Q. An, Z. Zeng, J. Wang, S. Deng, Boosting CO₂-to-CO conversion on a robust single-atom copper decorated carbon catalyst by enhancing intermediate binding strength, *J. Mater. Chem. A* 9 (2021) 1705–1712.
- [29] C. Bannwarth, S. Ehlert, S. Grimme, GFN2-xTB—an accurate and broadly parametrized self-consistent tight-binding quantum chemical method with multipole electrostatics and density-dependent dispersion contributions, *J. Chem. Theory Comput.* 15 (2019) 1652–1671.
- [30] H. Du, Q. Liu, N. Cheng, A.M. Asiri, X. Sun, C.M. Li, Template-assisted synthesis of CoP nanotubes to efficiently catalyze hydrogen-evolving reaction, *J. Mater. Chem. A* 2 (2014) 14812–14816.
- [31] P. Chen, N. Zhang, S. Wang, T. Zhou, Y. Tong, C. Ao, W. Yan, L. Zhang, W. Chu, C. Wu, Y. Xie, Interfacial engineering of cobalt sulfide/graphene hybrids for highly efficient ammonia electrosynthesis, *Proc. Natl. Acad. Sci. USA* 116 (2019) 6635–6640.
- [32] J. Wang, P. Zhang, L. Liu, Y. Zhang, J. Yang, Z. Zeng, S. Deng, Controllable synthesis of bifunctional porous carbon for efficient gas-mixture separation and high-performance supercapacitor, *Chem. Eng. J.* 348 (2018) 57–66.
- [33] Q. Zhou, Z. Shen, C. Zhu, J. Li, Z. Ding, P. Wang, F. Pan, Z. Zhang, H. Ma, S. Wang, H. Zhang, Nitrogen-doped CoP electrocatalysts for coupled hydrogen evolution and sulfur generation with low energy consumption, *Adv. Mater.* 30 (2018), 1800140.
- [34] F. Yang, X. Mao, M. Ma, C. Jiang, P. Zhang, J. Wang, Q. Deng, Z. Zeng, S. Deng, Scalable strategy to fabricate single Cu atoms coordinated carbons for efficient electroreduction of CO₂ to CO, *Carbon* 168 (2020) 528–535.
- [35] F. Yang, J. Wang, L. Liu, P. Zhang, W. Yu, Q. Deng, Z. Zeng, S. Deng, Synthesis of porous carbons with high N-content from shrimp shells for efficient CO₂-capture and gas separation, *ACS Sustain. Chem. Eng.* 6 (2018) 15550–15559.
- [36] S. Zhang, W. Gong, Y. Lv, H. Wang, M. Han, G. Wang, T. Shi, H. Zhang, A pyrolysis-phosphorization approach to fabricate carbon nanotubes with embedded CoP nanoparticles for ambient electrosynthesis of ammonia, *Chem. Commun.* 55 (2019) 12376–12379.
- [37] Y. Liu, Y. Zhu, J. Shen, J. Huang, X. Yang, C. Li, CoP nanoparticles anchored on N, P-dual-doped graphene-like carbon as a catalyst for water splitting in non-acidic media, *Nanoscale* 10 (2018) 2603–2612.
- [38] Z. Liang, W. Zhou, S. Gao, R. Zhao, H. Zhang, Y. Tang, J. Cheng, T. Qiu, B. Zhu, C. Qu, W. Guo, Q. Wang, R. Zou, Fabrication of hollow CoP/TiO_x heterostructures for enhanced oxygen evolution reaction, *Small* 16 (2019), 1905075.
- [39] H. Liao, Y. Sun, C. Dai, Y. Du, S. Xi, F. Liu, L. Yu, Z. Yang, Y. Hou, A.C. Fisher, S. Li, Z.J. Xu, An electron deficiency strategy for enhancing hydrogen evolution on CoP nano-electrocatalysts, *Nano Energy* 50 (2018) 273–280.
- [40] L. Jiao, Y.X. Zhou, H.L. Jiang, Metal–organic framework-based CoP/reduced graphene oxide: high-performance bifunctional electrocatalyst for overall water splitting, *Chem. Sci.* 7 (2016) 1690–1695.
- [41] S. Luo, X. Li, B. Zhang, Z. Luo, M. Luo, MOF-derived Co₃O₄@NC with core–shell structures for N₂ electrochemical reduction under ambient conditions, *ACS Appl. Mater. Interfaces* 11 (2019) 26891–26897.
- [42] X. Liu, H. Jang, P. Li, J. Wang, Q. Qin, M.G. Kim, G. Li, J. Cho, Antimony-based composites loading on phosphorus-doped carbon for boosting faradaic efficiency of the electrochemical nitrogen reduction reaction, *Angew. Chem. Int. Ed.* 58 (2019) 13329–13334.
- [43] W. Ye, Y. Yang, X. Fang, M. Arif, X. Chen, D. Yan, 2D cocrystallized metal–organic nanosheet array as an efficient and stable bifunctional electrocatalyst for overall water splitting, *ACS Sustain. Chem. Eng.* 7 (2019) 18085–18092.
- [44] D. Zhu, L. Zhang, R.E. Ruther, R.J. Hamers, Photo-illuminated diamond as a solid-state source of solvated electrons in water for nitrogen reduction, *Nat. Mater.* 12 (2013) 836–841.
- [45] Q.H. Wang, L.J. Yu, Y. Liu, L. Lin, R.G. Lu, J.P. Zhu, L. He, Z.L. Lu, Methods for the detection and determination of nitrite and nitrate: a review, *Talanta* 165 (2017) 709–720.
- [46] W. Ye, Y. Yang, M. Arif, S. Yang, X. Fang, M.A. Mushtaq, X. Chen, D. Yan, Fe, Mo–N/C hollow porous nitrogen-doped carbon nanorods as an effective electrocatalyst for N₂ reduction reaction, *ACS Sustain. Chem. Eng.* 8 (2020) 15946–15952.
- [47] C. Lv, Y. Qian, C. Yan, Y. Ding, Y. Liu, G. Chen, G. Yu, Defect engineering metal-free polymeric carbon nitride electrocatalyst for effective nitrogen fixation under ambient conditions, *Angew. Chem. Int. Ed.* 57 (2018) 10246–10250.
- [48] M. Wang, S. Liu, T. Qian, J. Liu, J. Zhou, H. Ji, J. Xiong, J. Zhong, C. Yan, Over 56.55% faradaic efficiency of ambient ammonia synthesis enabled by positively shifting the reaction potential, *Nat. Commun.* 10 (2019) 341.
- [49] M. Arif, G. Yasin, L. Lou, W. Ye, M.A. Mushtaq, X. Fang, X. Xiang, S. Ji, D. Yan, Hierarchical hollow nanotubes of NiFeV-layered double hydroxides@CoPV heterostructures towards efficient, pH-universal electrocatalytical nitrogen reduction reaction to ammonia, *Appl. Catal. B Environ.* 265 (2020), 118559.
- [50] S. Yang, W. Ye, D. Zhang, X. Fang, D. Yan, Layered double hydroxide derived bimetallic nickel–iron selenide as an active electrocatalyst for nitrogen fixation under ambient conditions, *Inorg. Chem. Front.* 8 (2021) 1762–1770.
- [51] J. Wu, Z. Wang, S. Li, S. Niu, Y. Zhang, J. Hu, J. Zhao, P. Xu, FeMoO₄ nanorods for efficient ambient electrochemical nitrogen reduction, *Chem. Commun.* 56 (2020) 6834–6837.
- [52] S. Zhang, M. Jin, T. Shi, M. Han, Q. Sun, Y. Lin, Z. Ding, L.R. Zheng, G. Wang, Y. Zhang, H. Zhang, H. Zhao, Electrocatalytically active Fe-(O-C₂)₄ single-atom sites for efficient reduction of nitrogen to ammonia, *Angew. Chem. Int. Ed.* 59 (2020) 13423–13429.
- [53] D. Wakerley, S. Lamaison, F. Ozanam, N. Menguy, D. Mercier, P. Marcus, M. Fontecave, V. Mougel, Bio-inspired hydrophobicity promotes CO₂ reduction on a Cu surface, *Nat. Mater.* 18 (2019) 1222–1227.
- [54] S.Z. Andersen, V. Čolić, S. Yang, J.A. Schwalbe, A.C. Nielander, J.M. McEnaney, K. E. Rasmussen, J.G. Baker, A.R. Singh, B.A. Rohr, M.J. Statt, S.J. Blair, S. Mezzavilla, J. Kibsgaard, P.C.K. Vesborg, M. Cargnello, S.F. Bent, T.F. Jaramillo, I.E.L. Stephens, J.K. Norskov, I. Chorkendorff, A rigorous electrochemical ammonia synthesis protocol with quantitative isotope measurements, *Nature* 570 (2019) 504–508.
- [55] B.H.R. Suryanto, H. Du, D. Wang, J. Chen, A.N. Simonov, D.R. MacFarlane, Challenges and prospects in the catalysis of electroreduction of nitrogen to ammonia, *Nat. Catal.* 2 (2019) 290–296.
- [56] K. Chu, Y. Liu, Y. Cheng, Q. Li, Synergistic boron-dopants and boron-induced oxygen vacancies in MnO₂ nanosheets to promote electrocatalytic nitrogen reduction, *J. Mater. Chem. A* 8 (2020) 5200–5208.
- [57] Q. Liu, X. Zhang, J. Wang, Y. Zhang, S. Bian, Z. Cheng, N. Kang, H. Huang, S. Gu, Y. Wang, D. Liu, P.K. Chu, X.F. Yu, Crystalline red phosphorus nanoribbons: large-scale synthesis and electrochemical nitrogen fixation, *Angew. Chem. Int. Ed.* 59 (2020) 14383–14387.
- [58] S. Liu, H.B. Yang, S.F. Hung, J. Ding, W. Cai, L. Liu, J. Gao, X. Li, X. Ren, Z. Kuang, Y. Huang, T. Zhang, B. Liu, Elucidating the electrocatalytic CO₂ reduction reaction over a model single-atom nickel catalyst, *Angew. Chem. Int. Ed.* 59 (2020) 798–803.
- [59] D. Masheder, K.P.J. Williams, Raman spectro-electrochemistry II: in situ raman spectroscopic studies of the electrochemical reduction of CO₂ at cobalt(II) phthalocyanine-impregnated PTFE-bonded carbon gas diffusion electrodes, *J. Raman Spectrosc.* 18 (1987) 391–398.
- [60] A. Li, Q. Cao, G. Zhou, B.V.K.J. Schmidt, W. Zhu, X. Yuan, H. Huo, J. Gong, M. Antonietti, Three-phase photocatalysis for the enhanced selectivity and activity of CO₂ reduction on a hydrophobic surface, *Angew. Chem. Int. Ed.* 58 (2019) 14549–14555.